AGU PUBLICATIONS

Geophysical Research Letters

RESEARCH LETTER
10.1002/2016GL069600

Anne Deschamps passed away on 26 December 2014; as PI she played a major role in designing and conducting the experiment.

Key Points:
- A seafloor monitoring experiment was initiated to quantify deformation across the Istanbul-Silivri segment of the North Anatolian Fault
- The first 6 months of data indicate no significant seafloor deformation across the fault
- Forward modeling suggests that the fault segment was partially or completely locked during the measurement period

Supporting Information:
- Supporting Information S1

Correspondence to:
V. Ballu,
valerie.ballu@univ-lr.fr

Citation:
Sakic, P., et al. (2016), No significant steady state surface creep along the North Anatolian Fault offshore Istanbul: Results of 6 months of seafloor acoustic ranging, *Geophys. Res. Lett.*, *43*, 6817–6825, doi:10.1002/2016GL069600.

Received 15 MAY 2016
Accepted 20 JUN 2016
Accepted article online 21 JUN 2016
Published online 2 JUL 2016

No significant steady state surface creep along the North Anatolian Fault offshore Istanbul: Results of 6 months of seafloor acoustic ranging

P. Sakic[1], H. Piété[2], V. Ballu[1], J.-Y. Royer[2], H. Kopp[3], D. Lange[3], F. Petersen[3], M. S. Özeren[4], S. Ergintav[5], L. Geli[6], P. Henry[7], and A. Deschamps[2]

[1]Laboratoire Littoral Environnement et Sociétés, Université de La Rochelle and CNRS, La Rochelle, France, [2]Laboratoire Géosciences Océan, Université de Brest and CNRS, Plouzané, France, [3]FB4 Dynamik des Ozeanbodens, GEOMAR Helmholtz-Zentrum für Ozeanforschung, Kiel, Germany, [4]Eurasian Institute of Earth Sciences, Istanbul Teknik Üniversitesi, Istanbul, Turkey, [5]Kandilli Observatory and Earthquake Research Institute, Department of Geodesy, Bogazici University, Istanbul, Turkey, [6]Laboratoire Aléas géologiques et Dynamique sédimentaire, UR Géosciences Marines, IFREMER, Institut Carnot EDROME, Plouzané, France, [7]CEREGE, Aix Marseille Université CNRS IRD and Collège de France, Aix en Provence, France

Abstract The submarine Istanbul-Silivri fault segment, within 15 km of Istanbul, is the only portion of the North Anatolian Fault that has not ruptured in the last 250 years. We report first results of a seafloor acoustic ranging experiment to quantify current horizontal deformation along this segment and assess whether the segment is creeping aseismically or accumulating stress to be released in a future event. Ten transponders were installed to monitor length variations along 15 baselines. A joint least squares inversion for across-fault baseline changes, accounting for sound speed drift at each transponder, precludes fault displacement rates larger than a few millimeters per year during the 6 month observation period. Forward modeling shows that the data better fit a locked state or a very moderate surface creep—less than 6 mm/yr compared to a far-field slip rate of over 20 mm/yr—suggesting that the fault segment is currently accumulating stress.

1. Introduction

The North Anatolian Fault (NAF) is a major right-lateral strike-slip fault accommodating 20–27 mm/yr relative motion between the Anatolia and Eurasia Plates [e.g., *Hergert and Heidbach*, 2010]. Over the past century, the NAF has produced major damaging earthquakes along most of its extent, except in the Marmara Sea [e.g., *Sengor et al*., 2005] (Figure 1). To the east, ruptures have propagated toward Istanbul since 1939, with a last event of magnitude 7.4 in Izmit in 1999 [e.g., *Barka et al*., 2002]. To the west, the NAF failed in 1912 in Ganos (*M*7.4 event) [e.g., *Aksoy et al*., 2010]. In the central Marmara Sea, the 70 km long Istanbul-Silivri segment (ISS) of the NAF has had no significant seismic events since at least 1766 and perhaps as far back as 989 [*Ambraseys*, 2002]. The probability of rupture of NAF segments in the central part of the Marmara Sea is considered to be significant [*Murru et al*., 2016; *Aochi and Ulrich*, 2015; *Parsons*, 2004], and *Schmittbuhl et al*. [2015] recently interpreted the low level of present-day seismicity along the ISS as the signature of a locked behavior. Although *Bohnhoff et al*. [2016] suggest that the maximum expected earthquake in the Istanbul area would probably not exceed a magnitude 7.5, geomechanical models generally predict high strain accumulation along the ISS, sufficient to produce a magnitude 7+ event [*Hergert and Heidbach*, 2010; *Pondard et al*., 2007; *Armijo et al*., 2005; *Le Pichon*, 2003]. Conversely, *Ergintav et al*. [2014] proposed that the ISS is aseismically creeping with strain accumulation less than 2 mm/yr, based on GPS data from distant and sparsely distributed land stations. Assessing whether the ISS is locked or aseismically creeping is crucial for estimating its seismic hazard potential and a major challenge using conventional methods.

Acoustic ranging has been successfully used to measure local deformation on the seafloor for more than a decade, in different geodynamic contexts and with resolutions ranging from centimeters to millimeters, mostly in seafloor spreading environments [e.g., *Burgmann and Chadwell*, 2014; *Osada et al*., 2012; *Chadwick and Stapp*, 2002; *Chadwell et al*., 1999; *Chadwick et al*., 1999].

In October 2014, during the Marsite cruise (R/V *Pourquoi Pas*?), we installed a ranging network of 10 acoustic transponders across the Istanbul-Silivri fault segment (Figure 1) at a depth of about 800 m, for up to 5 years. The targeted fault segment was identified using high-resolution mapping from utonomous Underwater

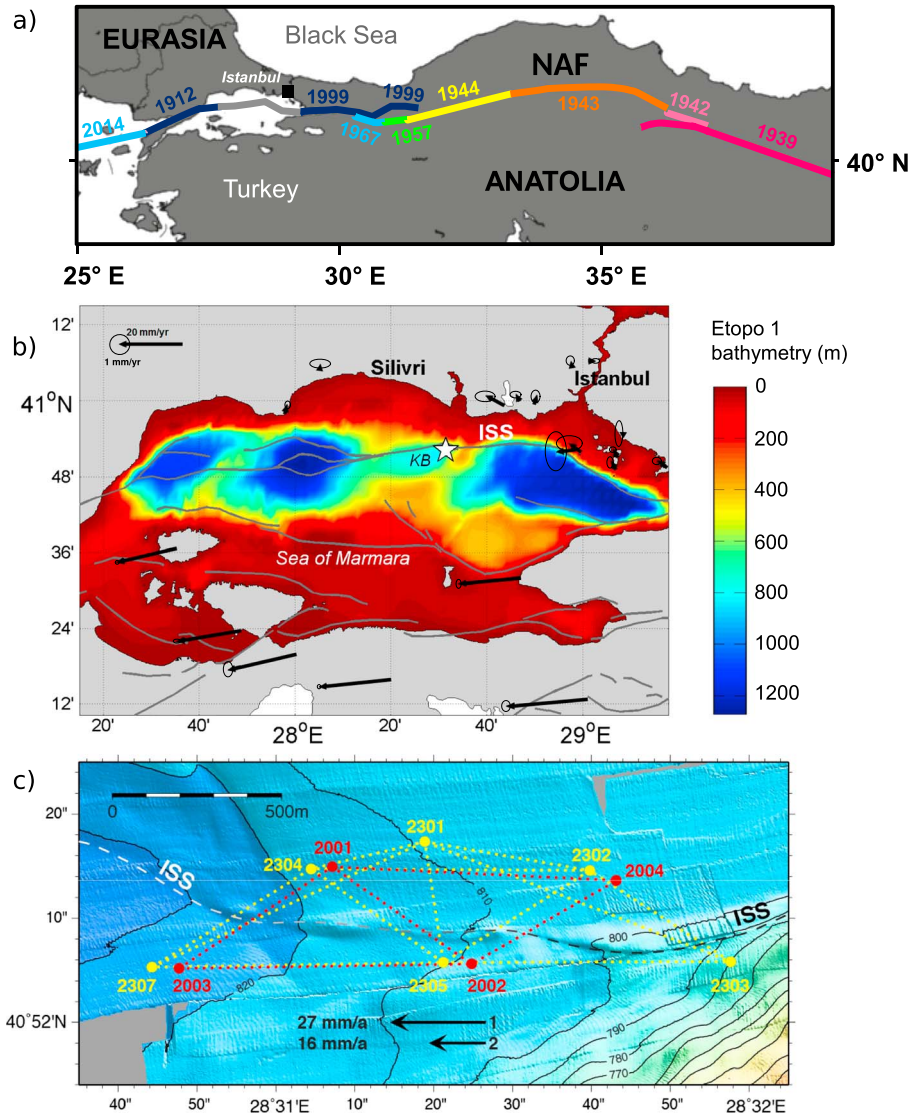

Figure 1. (a) Rupture zones associated with twentieth century major earthquakes along the NAF [after *Yamamoto et al.*, 2015; *Sengor et al.*, 2005]. (b) Position of the offshore geodetic network (white star) on the Istanbul-Silivri segment (ISS) in the Kumburgaz Basin (KB). The North Anatolian Fault traces (black lines) are after *Armijo et al.* [2002]. Arrows with 95% confidence ellipses represent the velocity field derived from permanent GPS stations, relative to stable Eurasia [*Ergintav et al.*, 2014]. (c) Layout of the offshore geodetic network, overlain on a high-resolution AUV bathymetry map [*Geli and Henry*, 2009]. Dotted lines show the monitored baselines between F (red) and G (yellow) transponder networks. The trace of the ISS (long dashed line) is outlined by an alignment of small sedimentary mounds. Vectors show the predicted strike-slip motion of Anatolia relative to Eurasia along the ISS by (1) *Reilinger et al.* [2006] and (2) *Hergert and Heidbach* [2010].

Vehicule (AUV), which revealed the existence of aligned, <3 m high, sedimentary mounds within the northeastern extremity of the Kumburgaz Basin (Figure 1c). It is assumed that these sedimentary beads outline the active trace of the fault [*Sengor et al.*, 2014; *Grall*, 2013].

In this paper we present the first results of this long-term experiment, based on the first ~6 months of data retrieved in April 2015 during cruise POS484 (R/V *Poseidon*). To take full advantage of the many baselines this subsea geodetic network provides, we developed a new methodology to constrain deformation based on a least squares inversion of the measured traveltimes. We first describe the data and their processing. We then present the inversion method and its results. Finally, we use forward modeling to provide bounds on the seafloor deformation during the measurement period.

2. Data Collection and Processing

The geodetic array consists of two independently operating subnetworks (Figure 1): four transponders from the University of Brest, France (Network F, stations ID 2001 to 2004), and six transponders from the GEOMAR Institute, Germany (Network G, stations ID 2301 to 2307). The layout results in 15 monitored baselines, of which five are measured by colocated F and G units for redundancy and to compare the equipment behavior in a long-term deployment. The transponders (Sonardyne Autonomous Monitoring Transponders, AMT) are mounted on top of 3.6 m high tripods to keep acoustic paths well above the seafloor despite near-bottom refraction. The tripods were deployed on the seafloor with a cable from the ship. Transponders use 8 ms phase-coded pulses, with an 8 kHz bandwidth centered at 22.5 kHz (F units) or 17.0 kHz (G units). Ranges are calculated by cross correlating the expected and received signals with a 0.5 ms resolution (submillimeter equivalent). In addition to hourly (F network) or bihourly (G network) baseline measurements, the instruments record water sound speed, pressure, temperature, and tilt along two orthogonal axes. Each transponder unit wakes up successively in a master mode (interrogating) and in a slave mode (responding), which results in multiple sets of baseline measurements collected in similar environmental conditions (see details on array configuration in Table S1 in the supporting information). The experiment is designed to last for the duration of the batteries, expected to be 3 years for G stations and 5 for the F stations. The sampling strategy was adjusted to minimize the power consumption. Data, stored in each station, can be downloaded from the surface with an acoustic modem, as well as the battery status; if needed, any station can be reconfigured from the surface.

In April 2015, the first 160 days of baseline ranging were acoustically downloaded from the transponders. The data processing starts by converting time of flight between transponder pairs into baseline distances, which requires sound speed information along the acoustic path. The sound speed sensors mounted on each AMT proved to be unusable due to repeated instrumental offsets and continuous drift induced by frequent cold water pulses in the Marmara Sea [e.g., *Book et al*., 2014; *Jarosz et al*., 2011]. We therefore recalculated sound speeds using *Del Grosso*'s [1974] formula based on temperatures and pressures recorded at each transponder and assuming an average salinity of 38.65 practical salinity unit derived from available historical data [*Boyer et al*., 2013]. Sound speed along the complete raypath is approximated by the harmonic mean of the sound speed at the two endpoints.

As shown by the temperature records (supporting information Figure S6), the deep waters of the Kumburgaz Basin show little variability over time, except for 0.5 to 2 day long abrupt cold events occurring every 6 to 21 days and corresponding to a ~0.02 °C temperature decrease, significant for a deep and otherwise isothermal environment [*Besiktepe et al*., 1994]. These events create distinct spikes in the acoustic traveltimes which translate to centimeter size spikes in the converted ranges. After discarding these cold event periods (which represent between 4% and 20% of the measurements) and removing outliers using a median absolute deviation method [*Rousseeuw and Croux*, 1993], rangings on individual baselines have an average 1 sigma standard deviation of 2.1 mm for all baselines over the 6 months.

Inclinometer data show that the tripods are quasi-vertical, and remained relatively stable, within the sensor resolution (10^{-3} rad = 0.057°), throughout the observation period (supporting information Figure S7). Only the F beacons could be oriented during a remotely operated vehicle inspection of the array and thus corrected for inclination variations. Such correction is not possible for the G transponders, randomly oriented relative to the tripods (supporting information Figure S1). The largest variation in the F network is recorded by unit F-2004 with a gradual 0.11° tilt over the 6 month period, probably due to the settling of the structure into the soft seabed. The resulting range error on the two affected baselines (2001–2004 and 2002–2004) does not exceed 2 mm in 6 months, due to the favorable tilt orientation. For the other F baselines, however, the tilt effect reached up to 4 mm in 6 months but is accounted for in the processing.

Changes in baseline length may result from a combination of true length variations and drift in the computed sound speeds used in the time-to-distance conversion. Although the relationship between temperature, pressure, and sound speed is not linear [*Del Grosso*, 1974], if temperature and pressure measurements drift linearly within the manufacturer's specifications (respectively 6.5–8.5 ppm/yr and 7 ppm/yr), the derived sound speed drifts linearly to first order, at a rate of less than 2.6×10^{-5} m/s/yr. In the next section, we propose a least squares inversion, which accounts for this potential observation bias, with the objective of providing bounds on the fault motion over the 160 days of measurements.

3. Data Modeling

Baseline lengths were first computed using sound speeds derived from in situ temperature and pressure sensors, assuming that these sensors did not drift. The results show significant variations in baseline trends, with a 1 sigma standard deviation of 15.4 mm/yr around an average value of −0.61 mm/yr. However, the deformation pattern is inconsistent, i.e., with inconsistent changes in parallel baselines or in crossed baselines, and discrepancies between redundant F and G baseline trends (although traveltime records at colocated F and G units display similar long-term trends). These inconsistencies are interpreted as evidence of unknown instrumental drifts in the temperature sensors, which must then be treated as variables and jointly estimated with the baseline changes. To address and simplify this problem, further modeling will be based on two main hypotheses: a simple behavior of the in situ temperature and pressure sensors (i.e., linear drift of the sound speed derived from these sensors) and a simple strain model based on the geological setting (deformation is assumed to localize along the fault trace with no strain on either side of the fault). For this first-order modeling, any apparent trend in a baseline that does not cross the fault is interpreted to result only from sound speed drift at the bounding transponders.

3.1. Least Squares Inversion

3.1.1. Inversion Procedure

We designed a nonlinear least squares inversion to simultaneously determine the two sets of independent variables: sound speed drift at each site and baseline length variation between sites. Input observations are sound speeds (derived from measured pressure and temperature) at each site and acoustic traveltimes between site pairs. Based on the elementary relation $\tau = \frac{d}{c}$ where τ is the one-way traveltime, c the sound speed, and d the baseline length between a transponder pair, the observation equation for each pair of transponders A and B is

$$\tau_{\text{theo},i,A\to B} = \frac{1}{2}\left(d_{0,A\to B} + \varphi_{A\leftrightarrow B} t_i\right).\left(\frac{1}{c'_{A,i} + k_A.t_i} + \frac{1}{c'_{B,i} + k_B.t_i}\right)$$

with

$\tau_{\text{theo},i,A\to B}$ the theoretical one-way traveltime (s) from transponder A to transponder B at epoch i,
$d_{0,A\to B}$ the initial baseline length (m) between transponders A and B at the reference epoch,
$\varphi_{A\leftrightarrow B}$ the (constant) deformation rate (m/yr) of the baseline length between transponders A and B,
t_i the epoch (year) of the ping relative to the reference,
k_A, k_B the coefficients of the sound speed linear drift (m/s/yr) for transponders A and B, respectively, and
$c'_{A,i}$, $c'_{B,i}$ the computed sound speed (m/s) at transponders A and B at epoch i.

The objective is to minimize the difference between the observed traveltimes and the predicted ones in a least squares sense. Changes in baselines are treated in three different ways: they are either unconstrained ("free mode"); set to a given value, for instance, zero, ("fixed mode"); or constrained to tend toward a given value with a chosen uncertainty or weight ("constrained mode"). These conditions are differently applied to baselines crossing the fault or not crossing the fault, since we assume that all strain occurs across the fault.

To avoid excessive and unrealistic sensor drift parameters, we force the drift coefficients, k, to tend toward zero with a σ_k standard deviation, where σ_k is set to 2.6×10^{-5} m/s/yr based on the manufacturer's temperature and pressure sensor drift uncertainties (9 ppm/yr and 7 ppm/yr, respectively). A single sound speed is computed for colocated transponders, generally based on the G station sensors for consistency.

Details of the inversion procedures are provided in the supporting information.

3.1.2. Inversion Results

We present results for inversions with different configurations. Sensor drift parameters, k, were either let free or constrained toward zero, with a standard deviation as defined above. Similarly, the deformation parameters, φ, were either fixed at zero or constrained to tend toward zero for the baselines on either side of the fault and let free or constrained to tend toward the slope of the linear regression fitting the raw time series (in order not to depart excessively from initial trends), for the fault-crossing baselines.

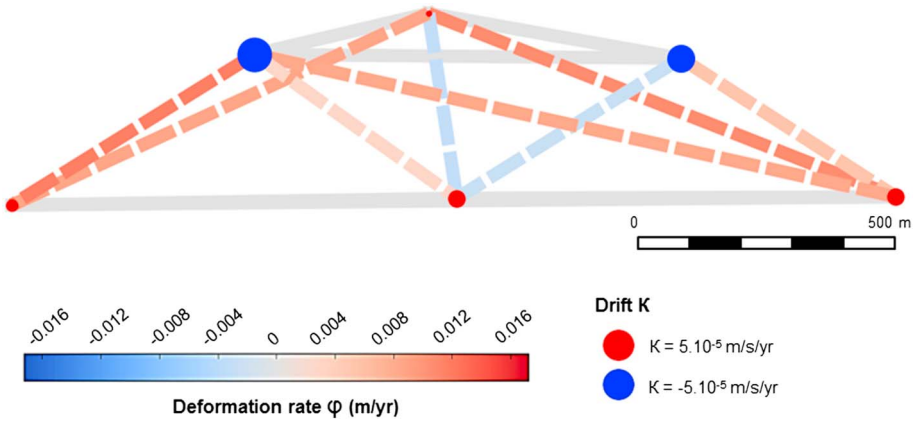

Figure 2. Rates of baseline changes obtained from a least squares inversion of baseline and sound speed data, with both constrained sensor drift (k) and baseline deformation rate (ϕ), i.e., assuming no strain on either sides of the fault (paths represented by grey lines). Deforming baselines are shown by dashed lines; colors indicate the magnitude and sign of baseline length variation. Drift in the sound speeds is represented by circles of size proportional to the drift magnitude.

Figure 2 illustrates the result for a joint inversion of sound speeds and ranging data when both k and φ are constrained. Illustrations for other cases are given in the supporting information (Figure S8), together with Table S2 of resulting φ and k values. The determined k and φ coefficients are within reasonable ranges: 10^{-5} to 10^{-6} m/s/yr and 1.5 to 9.7 mm/yr, respectively. However, baselines across the fault either lengthen or shorten inconsistently and show no significant trend, such as a consistent lateral strike-slip motion along the NAF. The results show that the horizontal surface motion across the fault is either zero or too small during the observation period to be detected. Without further constraints, a consistent and meaningful deformation pattern across the NAF cannot yet be extracted.

This 6 month limited data set may, however, provide an upper bound on the strike-slip motion along the ISS segment of the NAF. In the following, we propose an alternative approach based on the comparison of the observed baseline changes with those predicted for a range of slip rates.

3.2. Optimal Slip Rate Estimate Using Forward Modeling

Our forward modeling approach searches for the fault slip rate that best fits the data, assuming a simple, east-west oriented, surface-creeping strike-slip fault passing through the geodetic array. For slip rates v ranging from −20 mm/yr to 20 mm/yr, one can predict a theoretical change $\varphi_{i,v}$ on each baseline i, based on the geometry of the transponders (Figure 1). In the following, positive slip rates mean right-lateral strike-slip motion along the NAF.

The predicted $\varphi_{i,v}$ are then used as a priori values in the least squares inversion, using the constraining approach described in the supporting information. The weight p_φ on the baseline length variations is set high (corresponding to a standard deviation $\sigma_\varphi = 10^{-6}$ m/yr), so that the inversion is forced toward the forward model, and the k drift parameters are constrained toward 0 to keep drift estimates within reasonable bounds.

The fit between the forward model and the observations is quantitatively assessed using three criteria. The first criterion is the normalized residual sum of squares. The second criterion is based on the comparison of the $\varphi_{i,v}$ from the forward model with the slope $f_{i,v}$ of the range time series output of the inversion (range corrected for sound speed drift), for the n baselines. For a slip rate v in the forward model, we defined $\Delta\Phi_v$ as the root-mean-square (RMS) of the differences between $\varphi_{i,v}$ and $f_{i,v}$, which can be written as $\Delta\Phi_v = \sqrt{\frac{1}{n}\sum_{i=1}^{n}\left(\varphi_{i,v} - f_{i,v}\right)^2}$. The third criterion is the RMS of the k parameters, which is expected to be sufficiently small to ensure that drift values stay within reasonable ranges. The latter two criteria are averaged over all baselines. To make sure that no baseline is outside of reasonable range, we also provide the maximum values obtained for both criteria.

Figure 3 shows how these criteria vary with imposed slip rates. Observations are best modeled for slip rates close to 0 mm/yr and poorly modeled for strike-slip rates exceeding 10 mm/yr, for which all criteria

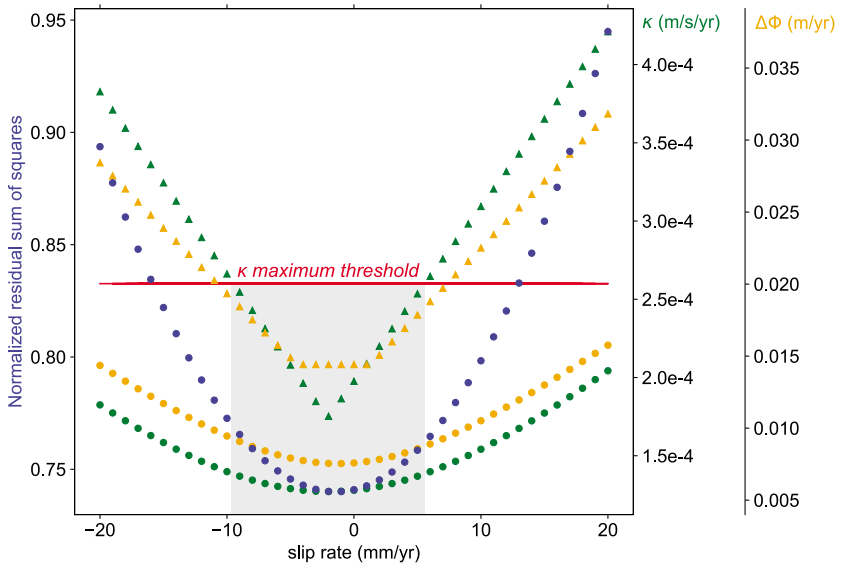

Figure 3. Criteria (*y* axis) illustrating the quality of fit between observations and predicted deformation on a pure strike-slip fault creeping with various slip rates (*x* axis). These criteria are the normalized residual sum of squares (blue circles), the baseline slope misfit $\Delta\Phi_v$ (orange circles/triangles), and the RMS of *k* parameters (green circles/triangles). Circles indicate the RMS value of the considered parameter averaged for all baselines, and triangles indicate its maximum value. The highlighted (grey area) range of possible slip rates is defined by the maximum sound speed drift (red line) satisfying the manufacturers' specifications (above this line, *k* estimates become unrealistic).

significantly depart from the minimum flat zone and reach a maximum for the highest tested slip rates of 20 mm/yr. It is worth noting that although they are not directly linked, the three criteria give similar results. Slip rates higher than 6 mm/yr yield drifts (*k*) that would exceed the manufacturers' specifications for the temperature and pressure sensors.

The best fitting negative slip rate of about −2 mm/yr (i.e., left lateral) is unexpected but probably not significant. We performed a Monte Carlo test to evaluate the uncertainty in this best fitting slip rate, randomly subsampling 1% of the traveltimes between each beacon pairs and using these subsets as input in the forward modeling. The operation was repeated 20 times to obtain a range of optimal slip rates. The corresponding 1 sigma standard deviation for the optimal slip rate is 1.57 mm/yr, using the $\Delta\Phi_v$ criterion (second criterion above) and 0.69 mm/yr using the normalized residual sum of squares (first criterion above).

4. Discussion

Based on a first-order modeling of the ISS motion, our inversion shows that during the observation period (160 days) the surface motion along the fault segment was too small to be detected, given the measurement uncertainties. Forward modeling, however, appears to preclude any displacement of the fault in excess of a few mm/yr.

It is likely that the first weeks of the experiment constitute a transitional period, during which sensors and onboard electronics adapt to the underwater environment and during which tripods settle on the seafloor. Instability of the geodetic structures can pose a significant problem for ranging methods [e.g., *McGuire and Collins*, 2013]. In this study, we were able to correct for the inclination of the F units, but not for the G stations, since their inclinometers have unknown orientations; in addition, the attitude data have a limited resolution (0.057°). The most significant tilt variations are observed on G-2303; this station, installed on the bounding slope of the basin, had an initial 9° tilt from vertical. Oscillations in the orthogonal tilt components would translate into a range error of several centimeters (i.e., several milliseconds) for the 3.60 m high tripod. But since baselines bounded by this unit do not display such variations, it probably means that only the transponder is oscillating.

Another limitation in monitoring this fault motion could be inherent to the network layout. Due to topographic constraints and limitations in the maximum acoustic range, units south of the ISS are located very

close to the fault (Figure 1c). Previous on-land studies of NAF segments demonstrated that significant deformation caused by aseismic creeping can be detected at short distances (~0.1 km) from the fault, when deformation is localized [*Ozener et al*., 2013]. In the survey area, the main fault trace is visible on subbottom profiles, and in the high-resolution bathymetry, where it is marked by an alignment of $<$3 m high sedimentary beads [e.g., *Sengor et al*., 2014] (Figure 1c), suggesting a narrow deformation zone. However, part of the deformation could be distributed, in a swath about 1 km wide south of the main fault trace, where deformation is observed in the sediments at shallow depths, and along other, less active, fault traces observed north of the survey area. However, based on geomorphologic expression, slip rates on these secondary faults are expected to be much smaller than on the main fault [e.g., *Sengor et al*., 2014; *Sorlien et al*., 2012; *Le Pichon et al*., 2001].

In our first-order modeling, the motion on the fault is approximated by a pure strike-slip motion, with a constant creep rate, which provides a reasonable description without any a priori knowledge on the expected deformation, in view of the limited data available. However, subsurface sediment deformation suggests a more complex deformation pattern with a small shortening component, perpendicular to the fault [*Demirbag et al*., 2003]. A N160-oriented normal fault scarp is observed 150 m west of unit G-2304, which indicates that extension occurs nearly parallel to the strike-slip fault crossing the Kumburgaz Basin [*Grall*, 2013]. Southwest of the network, deformation of sediments is likely associated with downslope creep that would potentially cause a shortening of the southern baselines parallel to the fault [*Zitter et al*., 2012; *Shillington et al*., 2012]. Nevertheless, no obvious evidence of such processes is found in the data.

Results from the forward modeling indicate that the Istanbul-Silivri segment did not creep, at least at the seafloor, more than a few millimeters during the observation period. This is significantly less than long-term slip rates predicted for the NAF in this area [*Flerit et al*., 2003; *Reilinger et al*., 2006; *Hergert and Heidbach*, 2010] or from distant on-land GPS data [*Ergintav et al*., 2014]. If this slip deficit corresponds to a steady state behavior of the fault, it implies that the NAF is currently accumulating stress at the surface. Over the width of the network, this information could help constraining the locking depth (see supporting information Figure S9); however, the current resolution is still insufficient to discriminate between shallow or deep estimates based on GPS or seismicity data [e.g., *Ergintav et al*., 2014; *Schmittbuhl et al*., 2015].

The 6 months of observations are best modeled by surface slip rates close to 0 mm/yr on the ISS of the NAF with an upper bound of 6 mm/yr to stay within reasonable limits for the sound speed drift. This maximum value is, however, compatible with the rates previously observed along the extensively monitored Ismetpasa section of the NAF on land, which aseismically creeps at rates of 7–8 mm/yr; however, the surface creep there likely results from postseismic afterslip [*Ozener et al*., 2013].

Compared to the steady state slip rate of 16 mm/yr estimated by *Hergert and Heidbach* [2010] for the NAF in this area, this result implies more than 10 mm/yr of strain accumulation. If the current slip rate is near steady state, this would correspond to slip deficits of over 2.5 m since the 1766 earthquake. Along a fault several tens of kilometers long, such slip deficits could generate an earthquake of magnitude $>$7, in agreement with other estimates of the earthquake hazard near Istanbul [*Bohnhoff et al*., 2016; *Murru et al*., 2016; *Armijo et al*., 2005; *Le Pichon et al*., 2001].

5. Conclusion

Data acquired during 6 months by a network of 10 acoustic transponders deployed along the submerged ISS segment of the NAF provide first insights into the fault segment behavior. Data inversion indicates that the deformation signal is smaller than the baseline resolution, which ranges between 1.5 and 2.5 mm for the measurement of horizontal distances up to several hundred meters. This suggests little or no surface deformation across the fault during the period of observation. Comparison of observed and predicted baseline changes obtained from a simple strike-slip model indicates that the surface slip rate across the Istanbul-Silivri segment is close to zero, with an upper bound of 6 mm/yr. If this behavior is steady state, the $>$10 mm/yr slip deficit implies that the Istanbul-Silivri segment of the NAF is currently accumulating stress that could be released in a major earthquake. Longer time series will either confirm this observation or show that the fault has a more complex behavior such as a stepwise creep.

Acknowledgments
The authors wish to thank the Captains and crews of R/V *Pourquoi Pas?* and R/V *Poseidon* for the successful deployment of the instruments [*Geli et al.*, 2001] and recovery of the first set of data (POS484 2015), respectively. The deployment cruise was organized in the framework of the European FP7 Marsite project. This experiment received support from Labex Mer in Brest (ANR 10-LABX-19) and from the French component (INSU-CNRS) of the EMSO European research infrastructure. Contributions during the deployment cruise from R. Apprioual, H. Ondréas, and L. Ruffine (Ifremer) and from C. Hammersley and T. Bennetts (Sonardyne Cie Limited) are greatly acknowledged. We also thank W. Crawford and O. de Viron for their discussions on the manuscript, as well as the Associate Editor A. Newman, W. Chadwick, and an anonymous reviewer for their constructive comments. P. Sakic was supported by a PhD grant from the French Ministry of Research/University of La Rochelle. H. Piété was funded under the Région Bretagne CANOPUS FUI project. Data are available upon request to the authors. This paper is dedicated to the memory of the Principal Investigator of this subsea geodetic project, Anne Deschamps, who passed away shortly after leading the successful deployment of the acoustic transponders.

References

Aksoy, M. E., M. Meghraoui, M. Vallee, and Z. Cakir (2010), Rupture characteristics of the AD 1912 Murefte (Ganos) earthquake segment of the North Anatolian Fault (western Turkey), *Geology*, *38*(11), 991–994, doi:10.1130/G31447.1.

Ambraseys, N. (2002), The seismic activity of the Marmara Sea region over the last 2000 years, *Bull. Seismol. Soc. Am.*, *92*(1), 1–18, doi:10.1785/0120000843.

Aochi, H., and T. Ulrich (2015), A probable earthquake scenario near Istanbul determined from dynamic simulations, *Bull. Seismol. Soc. Am.*, *105*(3), 1468–1475, doi:10.1785/0120140283.

Armijo, R., B. Meyer, S. Navarro, G. King, and A. Barka (2002), Asymmetric slip partitioning in the Sea of Marmara pull-apart: A clue to propagation processes of the North Anatolian Fault?, *Terra Nova*, *14*(2), 80–86.

Armijo, R., et al. (2005), Submarine fault scarps in the Sea of Marmara pull-apart (North Anatolian Fault): Implications for seismic hazard in Istanbul, *Geochem. Geophys. Geosyst.*, *6*, Q06009, doi:10.1029/2004GC000896.

Barka, A., et al. (2002), The surface rupture and slip distribution of the 17 August 1999 Izmit earthquake (*M* 7.4), North Anatolian Fault, *Bull. Seismol. Soc. Am.*, *92*(1), 43–60, doi:10.1785/0120000841.

Besiktepe, S. T., H. I. Sur, E. Ozsoy, M. A. Latif, T. Oguz, and U. Unluata (1994), The circulation and hydrography of the Marmara Sea, *Prog. Oceanogr.*, *34*(4), 285–334.

Bohnhoff, M., P. Martinez-Garzon, F. Bulut, and Y. Ben-Zion (2016), Maximum earthquake magnitudes along different sections of the North Anatolian fault zone, *Tectonophysics*, *674*, 147–165.

Book, J. W., E. Jarosz, J. Chiggiato, and S. Besiktepe (2014), The oceanic response of the Turksh Straits System to an extreme drop in atmospheric pressure, *J. Geophys. Res. Oceans*, *119*, 3629–3644, doi:10.1002/2013JC009480.

Boyer, T. P., et al. (2013), World Ocean Database 2013, NOAA Atlas NESDIS 72. Silver Spring, MD: S. Levitus, A. Mishonov.

Burgmann, R., and D. Chadwell (2014), Seafloor geodesy, *Annu. Rev. Earth Planet. Sci.*, *42*, 509–534.

Chadwell, C. D., J. A. Hildebrand, F. N. Spiess, J. L. Morton, W. R. Normak, and C. A. Reiss (1999), No spreading across the Juan de Fuca Ridge axial cleft during 1994–1996, *Geophys. Res. Lett.*, *26*(16), 2525–2528, doi:10.1029/1999GL900570.

Chadwick, W. W., and M. Stapp (2002), A deep-sea observatory experiment using acoustic extensometers: Precise horizontal distance measurements across a mid-ocean ridge, *IEEE J. Oceanic Eng.*, *27*(2), 193–201.

Chadwick, W. W., R. W. Embley, H. B. Milburn, C. Meinig, and M. Stapp (1999), Evidence for deformation associated with the 1998 eruption of Axial Volcano, Juan de Fuca Ridge, from acoustic extensometer measurements, *Geophys. Res. Lett.*, *26*(23), 3441–3444, doi:10.1029/1999GL900498.

Del Grosso, V. A. (1974), New equation for the speed of sound in natural waters (with comparisons to other equations), *J. Acoust. Soc. Am.*, *56*, 1084–1091.

Demirbag, E., C. Rangin, X. Le Pichon, and A. M. C. Sengor (2003), Investigation of the tectonics of the Main Marmara Fault by means of deep-towed seismic data, *Tectonophysics*, *361*(1–2), 1–19, doi:10.1016/S0040-1951(02)00535-8.

Ergintav, S., R. E. Reilinger, R. Cakmak, M. Floyd, Z. Cakir, U. Dogan, R. W. King, S. McClusky, and H. Ozener (2014), Istanbul's earthquake hot spots: Geodetic constraints on strain accumulation along faults in the Marmara seismic gap, *Geophys. Res. Lett.*, *41*, 5783–5788, doi:10.1002/2014GL060985.

Flerit, F., R. Armijo, G. C. P. King, B. Myer, and A. Barka (2003), Slip partitioning in the Sea of Marmara pull-apart determined from GPS velocity vectors, *Geophys. J. Int.*, *154*, 1–7.

Geli, L., and P. Henry (2009), Marmesonet cruise, RV Le Suroît, doi:10.17600/9020040.

Geli, L., L. Ruffine, and P. Henry (2014), Marsitecruise cruise, RV Pourquoi pas?, doi:10.17600/14000500.

Grall, C. (2013). La faille Nord-Anatolienne dans sa portion immergée en Mer de Marmara: Evolution du réseau de failles et migration de fluides, PhD dissertation, Université Aix-Marseille.

Hergert, T., and O. Heidbach (2010), Slip-rate variability and distributed deformation in the Marmara Sea fault system, *Nat. Geosci.*, *3*(2), 132–135, doi:10.1038/NGEO739.

Jarosz, E., W. J. Teague, J. W. Book, and S. Besiktepe (2011), On flow variability in the Bosphorus Strait, *J. Geophys. Res.*, *116*, C08038, doi:10.1029/2010JC006861.

Le Pichon, X. (2003), The North Anatolian Fault in the Sea of Marmara, *J. Geophys. Res.*, *108*(B4), 2179, doi:10.1029/2002JB001862.

Le Pichon, X., et al. (2001), The active Main Marmara Fault, *Earth Planet. Sci. Lett.*, *192*(4), 595–616, doi:10.1016/S0012-821X(01)00449-6.

McGuire, J. J., and J. A. Collins (2013), Millimeter-level precision in a seafloor geodesy experiment at the Discovery transform fault, East Pacific Rise, *Geochem. Geophys. Geosyst.*, *14*, 4392–4402, doi:10.1002/ggge.20225.

Murru, M., A. Akinci, G. Falcone, S. Pucci, R. Console, and T. Parsons (2016), $M \geq 7$ earthquake rupture forecast and time-dependent probability for the Sea of Marmara region, Turkey, *J. Geophys. Res. Solid Earth*, *121*, 2679–2707, doi:10.1002/2015JB012595.

Osada, Y., M. Kido, and H. Fujimoto (2012), A long-term seafloor experiment using an acoustic ranging system: Precise horizontal distance measurements toward detection of seafloor crustal deformation, *Ocean Eng.*, *51*, 28–33.

Ozener, H., A. Dogru, and B. Turgut (2013), Quantifying aseismic creep on the Ismetpasa segment of the North Anatolian Fault Zone (Turkey) by 6 years of GPS observations, *J. Geodyn.*, *67*, 72–77.

Parsons, T. (2004), Recalculated probability of $M >= 7$ earthquakes beneath the Sea of Marmara, Turkey, *J. Geophys. Res.*, *109*, B05304, doi:10.1029/2003JB002667.

Pondard, N., R. Armijo, G. C. P. King, B. Meyer, and F. Flerit (2007), Fault interactions in the Sea of Marmara pull-apart (North Anatolian Fault): Earthquake clustering and propagating earthquake sequences, *Geophys. J. Int.*, *171*(3), 1185–1197, doi:10.1111/j.1365-246X.2007.03580.x.

Reilinger, R., et al. (2006), GPS constraints on continental deformation in the Africa-Arabia-Eurasia continental collision zone and implications for the dynamics of plate interactions, *J. Geophys. Res.*, *111*, B05411, doi:10.1029/2005JB004051.

Rousseeuw, P. J., and C. Croux (1993), Alternatives to the median absolute deviation, *J. Am. Stat. Assoc.*, *88*(424), 1273–1283, doi:10.1080/01621459.1993.10476408.

Schmittbuhl, J., H. Karabulut, O. Lengliné, and M. Bouchon (2015), Seismicity distribution and locking depth along the Main Marmara Fault, Turkey, *Geochem. Geophys. Geosyst.*, *17*, 1525–2027, doi:10.1002/2015GC006120.

Sengor, A. M. C., O. Tuysuz, C. Imren, M. Sakinc, H. Eyidogan, G. Gorur, X. Le Pichon, and C. Rangin (2005), The North Anatolian Fault: A new look, *Annu. Rev. Earth Planet. Sci.*, *33*, 37–112, doi:10.1146/annurev.earth.32.101802.120415.

Sengor, A. M. C., C. Grall, C. Imren, X. Le Pichon, N. Ambraseys, P. Henry, H. Karabulut, and M. Siyako (2014), The geometry of the North Anatolian transform fault in the Sea of Marmara and its temporal evolution: Implications for the development of intracontinental transform faults, *Can. J. Earth Sci.*, *51*(3), 222–242, doi:10.1139/cjes-2013-0160.

Shillington, D. J., et al. (2012), Evidence for widespread creep on the flanks of the Sea of Marmara transform basin from marine geophysical data, *Geology*, *40*(5), 439–442, doi:10.1130/G32652.1.

Sorlien, C. C., et al. (2012), Uniform basin growth over the last 500 Ka, North Anatolian Fault, Marmara Sea, Turkey, *Tectonophysics*, *518*(January), 1–16, doi:10.1016/j.tecto.2011.10.006.

Yamamoto, Y., N. Takahashi, S. Citak, D. Kalafat, A. Pinar, C. Gurbuz, and Y. Kaneda (2015), Offshore seismicity in the western Marmara Sea, Turkey, revealed by ocean bottom observation, *Earth Planets Space*, *67*(September), doi:10.1186/s40623-015-0325-9.

Zitter, T. A. C., C. Grall, P. Henry, M. S. Ozeren, M. N. Cagatay, A. M. C. Sengor, L. Gasperini, B. M. de Lepinay, and L. Geli (2012), Distribution, morphology and triggers of submarine mass wasting in the Sea of Marmara, *Mar. Geol.*, *329*(November), 58–74, doi:10.1016/j.margeo.2012.09.002.